
This manuscript is a preprint and has been submitted for peer review process. This manuscript has not been accepted or undergone proof read. Subsequent versions of this manuscript may have different content. Please feel free to contact any of the authors directly. We welcome feedback!

1 How Topographic Slopes Control Gravity Spreading in Salt-bearing

2 Passive Margins: Insights from Analogue Modelling

3 Zhiyuan Ge^{1,2,3}, Matthias Rosenau⁴ and Michael Warsitzka⁵

4 ¹ State Key Laboratory of Petroleum Resources and Prospecting, China University of
5 Petroleum (Beijing), Beijing, 102249, China.

6 ² College of Geosciences, China University of Petroleum (Beijing), Beijing, 102249,
7 China.

8 ³ Department of Earth Science, University of Bergen, Allégaten 41, 5007 Bergen,
9 Norway.

10 ⁴ Helmholtz Centre Potsdam – GFZ German Research Centre for Geosciences, 14473
11 Potsdam, Germany

12 ⁵ Institute of Geophysics of the Czech Academy of Sciences, Boční II/1401, 141 31
13 Prague 4, Czech Republic

14 Corresponding author: Zhiyuan Ge (gezhiyuan@cup.edu.cn)

15 Abstract

16 Sediment progradation and spreading is a key process during gravity-driven, thin-
17 skinned deformation in salt-bearing passive margins. However, to what degree the size
18 and shape of a progradational sedimentary wedge control gravity-driven deformation is
19 still not clear. We use analogue modelling to compare two endmember configurations
20 constrained by critical wedge theory, in which the sediment wedge has different initial
21 depositional slopes: a 5° critical (stable) slope and a 27° unstable slope. In both
22 configurations, differential loading initiates spreading characterized by a basinward
23 migrating system of linked proximal extension and distal contraction with a
24 translational domain in between. With a critical frontal slope, the translational domain
25 expands as the contractional domain migrates forward with viscous flow evenly
26 distributed. With a steep frontal slope, both extensional and contractional domains
27 migrate at similar rate due to more localized viscous flow under the wedge toe
28 producing diagnostic structures of late extension overprinting early contraction. In both
29 cases, salt flow is dominated by Poiseuille flow with only a subordinate contribution
30 from Couette flow, contrasting to classical gravity gliding systems dominated by
31 Couette flow. Comparison with previous studies reveal similar structural styles and
32 viscous flow patterns. Our study highlights the geometric variations of sedimentary
33 wedges result in variable responses in gravity spreading systems. With a steep frontal
34 slope, the sediment wedge is more likely to collapse and develop spreading associated
35 structures. However, such steep slope systems may not be very common in salt-bearing
36 passive margins as they are less likely to occur in nature.

37 **1 Introduction**

38 Gravity-driven tectonic deformation has been widely observed in salt-bearing
39 passive margins (e.g. Allen et al., 2016; Brun and Fort, 2011; Fort et al., 2004; Peel,
40 2014; Rowan, 2020; Rowan et al., 2004; Vendeville, 2005) (Fig. 1). As the sediment
41 progrades and deforms under its own weight above a basal evaporite layer, a typical
42 linked system occurs with a zone of proximal extension and a corresponding zone of
43 distal contraction (e.g. Dooley et al., 2020; Fort et al., 2004; Rowan et al., 2004).
44 Despite sharing some common features, the gravity-driven failures usually display vast
45 variations of structural styles and associated basin evolution, such as those basins along
46 the south Atlantic margins and the neighboring basins in the east Mediterranean (Kukla
47 et al., 2018; Zucker et al., 2019). The variations are largely due to the multiple controls
48 involved in the gravity-driven deformation, from tectonics-induced deformation
49 occurring in the whole basin to local sediment-structure interactions (Howlett et al.,
50 2020; Ings et al., 2004; Rowan, 2020). Most controls can be attributed to one of the two
51 basic modes of gravity-driven deformation: 1. gravity gliding driven by the tilting of
52 the detachment layer (Fig. 1a); 2. gravity spreading associated with the collapse of a
53 progradational sediment wedge due to differential loading (Fig. 1b) (Brun and Fort,
54 2011; Peel, 2014; Rowan et al., 2004; Schultz-Ela, 2001). For example, thermal
55 subsidence and tectonic uplift contribute the gravity gliding, and sediment progradation
56 and retrogradation affect gravity spreading (Rowan, 2020; Rowan et al., 2004).

57 Various criteria exist in defining gravity-driven deformation. Peel (2014)
58 proposes the release of potential energy as the criteria to categorize gravity deformation
59 as gravity gliding releases energy by slope parallel movement and gravity spreading
60 release energy by deforming internally. The two types of viscous flow, namely the
61 Couette and Poiseuille flows, have been thought to be associated with gravity gliding
62 and gravity spreading, respectively (Brun and Fort, 2011; Gemmer et al., 2005).
63 However, using salt flow analysis, Weijermars and Jackson (2014) address the frequent
64 coexistence of Couette and Poiseuille flows in salt and, thus, the difficulty in
65 distinguishing gliding and spreading during gravity-driven deformation.

66 We here follow the definition proposed by Raillard et al. (1997), which directly
67 links the boundary conditions in analogue modelling with different modes of
68 deformation: basin tilting and sediment progradation control gravity gliding and
69 gravity spreading, respectively. However, even under such definition, there are
70 different views on whether or how gravity spreading dynamics can dominate a gravity-
71 driven salt tectonic system (e.g. Brun & Fort, 2011; Rowan et al., 2012). The ability of
72 gravity gliding in controlling salt tectonics has been relatively well studied. Analogue
73 modelling studies show that margin tilting alone is sufficient to drive pronounced
74 gravity gliding with typical structural styles of upslope extension and downslope
75 contraction (Brun and Fort, 2011; Cobbold and Szatmari, 1991; Dooley et al., 2020; Ge
76 et al., 2019a; Quirk et al., 2012). In contrast, gravity spreading systems show
77 considerable variations in structural style and basin evolution. For instance,
78 progradational wedges can form expulsion rollovers or extensional grabens under
79 different boundary conditions (Ge et al., 1997; McClay et al., 1998; Vendeville, 2005).

80 Analogue and numerical modelling studies have been focused on the influences
81 of various controls, including progradation rate, sedimentation pattern, sediment
82 transport direction as well as base-salt relief, on gravity spreading systems (Cohen and
83 Hardy, 1996; Ge et al., 1997; Gemmer et al., 2005; Krézsek et al., 2007; McClay et al.,
84 2003; McClay et al., 1998; Vendeville, 2005). However, little attention has been given
85 to how geometric variation of sedimentary wedges affect a gravity-spreading system.
86 In general, sedimentary progradational systems and their deposit are simplified and
87 simulated as wedge-shaped sediment cover (e.g. Cohen & Hardy, 1996; Ge et al., 1997;
88 Krézsek et al., 2007; McClay et al., 1998), with loosely defined sedimentological
89 meanings. For example, the progradational rate and thickness of a sedimentary wedge
90 are based on the interpolation of overall sediment cover thickness from a few sites in
91 the basin (e.g. Adam et al., 2012; McClay et al., 1998). Even when specified with some
92 sedimentological implications, variable frontal slope, which directly links the
93 sedimentary wedge shape and associated depositional systems, have not been explicitly
94 explored (e.g. Ge et al., 1997; Gemmer et al., 2005; Gradmann et al., 2009).

95 In this study, using analogue modelling, we investigate the structural and
96 kinematic evolution of a passive margin salt tectonic system driven solely by
97 progradation of sedimentary wedges. We hypothesize that a geometric variation in the
98 frontal slope impose an important boundary condition. Wedge geometry has an effect
99 on the force balance and the spreading dynamics of progradational wedges similar to
100 accretionary wedges (e.g. Mourgues et al., 2014) which is often analysed in the
101 framework of the critical coulomb wedge (or taper) theory (CWT, e.g. Dahlen, 1990).
102 Based on sedimentological constrains, we here focus on two wedge geometries, one
103 with a critically stable and another with an extensionally unstable frontal slope
104 according to CWT. Moreover, we apply salt flow analysis on the results to infer the salt
105 flow kinematics (e.g. Warsitzka et al., 2018) and include previous models with various
106 frontal slopes into our analysis. Our models demonstrate how geometric variation of
107 the progradational wedge is able to control the dynamics of a thin-skinned gravity-
108 spreading system. The results shed lights on some issues of gravity-spreading systems
109 in passive margins and provide additional application of critical taper theory and salt
110 flow analysis to salt tectonics in general.

111 **2 Materials and Methods**

112 2.1 Geometric implication of sedimentary wedges

113 Sedimentary systems in passive margins have complex sedimentological and
114 geomorphological features controlled by tectonics, basin morphonology, climate,
115 sediment supply and so on (Carvajal et al., 2009; Helland-Hansen et al., 2012; O'Grady
116 et al., 2000; Patruno and Helland-Hansen, 2018). In both physical and numerical
117 simulations, sedimentary systems have been modelled as a sedimentary wedge thinning
118 from proximal to distal with relatively smooth topographical slopes (Brun and Fort,
119 2011; Ge et al., 1997; Gemmer et al., 2005; Gradmann et al., 2009; Krézsek et al., 2007;
120 McClay et al., 2003; Vendeville, 2005). In natural passive margin basins, sedimentary
121 wedges typically have thicknesses of a few 100s to 1000s of metres (Carvajal et al.,

122 2009; Helland-Hansen et al., 2012; Patruno and Helland-Hansen, 2018), resulting in
123 typical natural depositional slopes of $<5^\circ$ (Carvajal et al., 2009; O'Grady et al., 2000;
124 Prather et al., 2017). However, in some cases, depositional slopes can be much steeper
125 and close to the local angle of repose. Sea level changes, tectonics, and carbonate
126 deposition can cause local slopes up to 30° (Prather et al., 2017; Ross et al., 1994;
127 Schlager and Camber, 1986). In the northern Gulf of Mexico, for instance, some of the
128 seafloor profiles crossing the salt-related structures show slopes of up to 20° (Lugo-
129 Fernández and Morin, 2004; Roberts et al., 1999). At a smaller scale, Gilbert-type deltas
130 usually have subaqueous slopes between $20\text{--}27^\circ$ (Nemec, 1990). Therefore, the natural
131 sedimentary systems seem to be characterised by two types of depositional slopes: the
132 gentle ones ($< 5^\circ$) and steep ones ($>5^\circ$, up to 30°), whereas the first type plays a
133 dominant role in continental margins (O'Grady et al., 2000).

134 2.2 Constraints from Critical Wedge Theory (CWT)

135 According to CWT, a stability criterion (criticality) can be defined for a brittle
136 wedge (with surface slope angle α) pushed along a detachment horizon (with dip angle
137 β), which is a function of its geometry or “taper” angle ($\alpha+\beta$), the (effective) basal and
138 internal strengths as well as the densities of the solid and pore fluid phases (e.g. Dahlen,
139 1990). In contrast to purely frictional wedges, we here constrain the basal strength from
140 the observed shear rates and the silicone viscosity to be very low and equivalent to an
141 effective friction angle of $<1^\circ$. Furthermore, we consider the detachment horizon to be
142 horizontal ($\beta=0$) in our models.

143 Plotting the stability criterion into a α vs. β diagram results in a stability field
144 and enclosed by a failure envelope, which represents the critical state geometry (Fig 2).
145 Geometries plotting above the envelope are extensionally unstable while geometries
146 below are contractionally unstable. Both wedges presented here tend to deform until
147 the critical geometry representing force balance is reached. From a static point of view,
148 any wedge slope above a viscous layer tends to relax to a very low taper ($<1^\circ$) due to
149 the low long-term strength of the viscous substratum (Davis & Engelder, 1985). In a
150 dynamic system, such as realized in the presented study, the deformation is
151 continuously driven by sediment progradation. Hence, the geometric evolution is
152 disturbed continuously.

153 Applying CWT suggests that gentle slopes of sedimentary wedge ($\sim 5^\circ$) are just
154 at or slightly beyond the verge of failure (i.e. in the critical state), whereas steep slopes
155 ($20\text{--}30^\circ$) are clearly in the extensionally unstable regime (Fig. 2a). Since the distance
156 to the stability envelope is proportional to the force imbalance, we consider the two
157 scenarios as representing endmembers of close to stable (or critical) and highly unstable
158 wedges collapsing under extension.

159 2.3 Experimental setup and procedure

160 To test the effect of wedge stability on spreading dynamics, we use an analogue
161 modelling approach that simulates complex salt tectonic evolution similar to previous
162 studies (e.g. Brun & Fort, 2011; Ge et al., 2019a, b; McClay et al., 1998; Vendeville,

163 2005). We use a mixture of quartz sand and foam glass spheres as the cover material to
164 achieve a reasonable density ratio of 1.16 between brittle and viscous layers (see Table
165 1). The brittle behaviour of this granular mixture (Warsitzka et al., 2019), is similar to
166 sands used in previous analogue modelling studies (e.g. Klinkmüller et al., 2016) and
167 to natural rocks (e.g. Byerlee, 1978). As an analogue of viscous salt, the silicone used
168 in this study (KORASILON G30M) behaves like a Newtonian fluid up to a strain rate
169 of about 10^{-2} s^{-1} , which is well beyond our experimental range (Rudolf et al., 2016). We
170 derive a geometric scaling ratio of 10^{-5} (i.e. 1 cm in the model \approx 1 km in nature) and a
171 time scaling ratio of $\sim 10^{-10}$ (i.e. 4 hours in the model \approx 1 Ma in nature) based on standard
172 scaling procedures for submarine salt tectonic systems (see Adam and Krezsek, 2012
173 and references within) (Table 1).

174 A basal sand body on top of a rigid basal plate forms the mould of two identical
175 silicone basins (Fig. 3). Compared to a setup with an even thickness silicone, the
176 double-wedge shape of the silicone base is a more realistic representation of a passive
177 margin salt basin (Brun and Fort, 2011; Zwaan et al., 2021). We note that the variation
178 in silicone thickness may lead, besides velocity variations, to spatial strength variations
179 within the viscous silicone. However, stability analysis shows that a spatial (or temporal)
180 variation of even one order of magnitude in basal strength has little impact upon the
181 stability fields (Fig. 2).

182 We test two syn-kinematic sedimentary wedges. Initially, the first model has a
183 critical slope of roughly 5° (Model 1) and the second model has a steep, unstable slope
184 of roughly 27° (Model 2). Both models start with sieving an even, 1 mm thick, pre-
185 kinematic sand layer over the silicone before further sedimentation is added (Fig. 3a).
186 Every 12 hours over a duration of 5 days, a maximum of 4 mm (Model 1) and 25 mm
187 (Model 2) are added (fig. 3a) to simulate syn-kinematic sediment progradation. For
188 simplicity, no lateral variations of sedimentation are considered.

189 Both wedges prograde basinward at the same rate of 10 cm day^{-1} ($\sim 10 \text{ km in 6}$
190 Ma) with an aggradational rate of 2 mm day^{-1} ($\sim 200 \text{ m in 6 Ma}$) (Fig. 3a), falling into
191 the slower end of natural progradational systems (e.g. Carvajal et al., 2009). Due to
192 constant progradational and aggradational rate, the frontal slope decreases to 2.6° in
193 Model 1 and increases to 34.2° in Model 2 towards the end of the experiment (Fig. 3a).
194 Thus, the stability analysis is still valid for both wedges during the experiment, although
195 the actual frontal slope may vary slightly due to sieving more sand in topographically
196 low areas (Fig. 2a). The variation of the progradational rate of the two wedges
197 represents two types of sedimentary system as the one in Model 1 has a relatively stable
198 shelf edge near the upslope basin boundary and the one in Model 2 has a fast migrating
199 shelf edge. Thus, the different geometries of the two wedges also reflect the variable
200 amounts of sediment input (Fig. 3).

201 During the experiment, the model surface is monitored with a stereoscopic pair
202 of cameras. Digital image correlation (DIC; LaVision Davis 8, see details in Ge et al.,
203 2020) applied on the stereoscopic images provides the 3D topography as well as
204 incremental displacement (or velocity) and strain fields of the model surface at high
205 spatial and temporal resolution (e.g. Adam et al., 2005). After the experiment, the

206 models are wetted, sequentially sliced, and photographed to provide cross-sectional
207 views.

208 2.4 Silicone flow analysis

209 Based on the surface deformation derived from the DIC, we calculate the flow
210 velocity field in the underlying silicone layer. We assume that the progradating sand
211 wedge induces (1) a Poiseuille channel flow in the viscous layer driven by lateral
212 differential loading (Fig. 4) and the resulting hydraulic head gradient (dP/dx) (Hudec
213 and Jackson, 2007; Kehle, 1988). The hydraulic head gradient consists of the
214 components of the pressure head gradient, produced by lateral changes of the sand layer
215 thickness on top of the silicone, and the elevation head gradient, caused by lateral
216 changes in the elevation of the top silicone. Furthermore, we suggest that the collapsing,
217 basinward sliding wedge causes horizontal shear stresses, which linearly decrease with
218 depth in the viscous layer inducing (2) a Couette shear flow component (Gemmer et al.,
219 2005). Based on steady-state solutions of the Navier-Stokes equation, we derive the
220 horizontal velocity u_x , consisting of flow components, by the following equation (e.g.
221 Turcotte and Schubert, 2014 as applied in Warsitzka et al., 2018):

$$222 \quad u_x = \frac{1}{2\eta} \frac{dP}{dx} (h_s^2 - z^2) + \frac{u_T}{h_s} \quad (\text{Eq. 1})$$

223 Here, η is the dynamic viscosity, h_s is the thickness of the silicone layer, z is the
224 depth, and u_T is the horizontal velocity at the top of the silicone layer. For simplicity,
225 we consider only the horizontal x -component of the hydraulic head gradient and the
226 flow velocity, which is reasonable when the viscous layer is not tilted during the
227 deformation. This computation bares the limitations that no deformation or strength of
228 the cover layer was included, which would tend to reduce flow velocities. Therefore,
229 the amounts of velocity calculated in our models are effectively the upper limits for
230 cases when no shear strength acts. Furthermore, the flow velocity fields illustrated here
231 should be considered instantaneous with no reflection of the dynamic redistribution
232 (advection) of the silicone (Warsitzka et al., 2018).

233 As geometric input, simplified shapes of the experimental layers are used based on
234 the DIC-derived digital topography (Fig. 4). We calculate the velocity for each phase,
235 after adding a new sand layer, which modifies the topography and, therefore, the
236 hydraulic head gradient. The downslope horizontal and the vertical DIC-derived
237 surface velocity components v_x and v_z are then used to calculate the translation of the
238 overburden, assuming that v_x at the top of the sand cover is equal to u_T at the base of
239 the cover. The vertical velocity component v_z is transferred to the top silicone interface
240 by an angle of 60° assuming that the overburden subsidence is translated to the base of
241 the cover by 60° -dipping normal faults (cf. Fig. 3). During the computation procedure,
242 the model is built with a grid of equidistant nodes (~ 1.5 mm distance). Then, the
243 hydraulic head gradient is calculated between each node and inserted into the equation
244 of the flow velocity u_x together with the measured velocity u_T (Eq. 1). Finally, the
245 velocity field is smoothed to filter out small-scale topographic irregularities.

246 **3 Experimental observations**

247 3.1 Model 1: Progradation With Critical Depositional Slope

248 In Model 1 (5° critically stable slope), the input of sand cover wedge
249 immediately triggers extension (Fig. 2a) occupying $\sim 10\%$ of the basin length (% b.l.)
250 and contraction affecting $\sim 20\%$ b.l. with a translational domain of $\sim 20\%$ b.l. in
251 between (Figs 5a & 6a). The extensional domain is characterised by two grabens (G1
252 and G2) while the contractional domain is composed of numerous small-wavelength
253 (1–2 cm) folds and thrusts (F1) (Figs 5a & 6a). After 24 hours, as the sand wedge
254 progrades basinward, an additional graben G3 occurs at 5 cm offset from G2, and an
255 additional fold set (F2) nucleates 5 cm away from F1 (Fig 3a). Simultaneously with the
256 development of new extensional and contractional structures, the translational domain
257 (TD) increases to $\sim 30\%$ b.l. as a part of the contractional domain gets buried and
258 becomes deactivated (Fig. 5a & 6a). Meanwhile the TD continues to spread
259 reaching $>50\%$ b.l. by the end of the experiment (Fig. 5a & 6a). As the translational
260 domain expands, the extensional domain increases to $>20\%$ b.l. until G1 deactivates
261 after 72 hours (Fig. 6a). In contrast, the contractional domain decreases to $\sim 10\%$ b.l.
262 after 64 hours until a new fold and thrust set F3 nucleates 10 cm offset from F2 (Fig.
263 6a). Contemporaneously with the occurrence of F3, a distal contractional structure F5
264 localizes at the basinward edge of the silicone basin, switching from its early
265 extensional nature (Fig. 6a). A final migration of the contraction occurs at 84 hours as
266 the fold and thrust set F4 develops c. 8 cm next to F3 (Fig. 6a).

267 3.2 Model 1: Progradation With Unstable Depositional Slope

268 In Model 2 (27° unstable slope), the sand wedge initiates three extensional
269 grabens (G1–G3) and a small-wavelength fold and thrust set (F1) covering $\sim 10\%$ b.l.
270 and $\sim 15\%$ b.l., respectively, with a translational domain (TD1) in between occupying
271 $<5\%$ b.l. (Fig. 5b & 6b). In contrast to Model 1, no deformation occurs in the most
272 landward area as spreading is localized at the wedge front (Fig. 6b). After 24 hours, a
273 new extensional graben occurs between the initial translational domain (TD1) and the
274 contractional domain, increasing the extensional domain to $\sim 15\%$ b.l. (Fig. 6b).
275 Another fold and thrust set F2 forms in the basinward side of F1, followed by F3–F5
276 between 24–36 hours, increasing the contractional domain to $\sim 40\%$ b.l. (Fig. 6b).
277 During the basinward migration of both domains, the early translational domain (TD1)
278 is overprinted by the extensional domain, while the fold and thrust set (F1) becomes
279 part of the new translational domain (TD2) (Fig. 6b). At 36 hours, contractional
280 structures (F7) localize in the basinward basin edge (Fig. 6b). Around the 60-hour mark,
281 an extensional graben (G5) occurs at the location of F2 and F3 while a distal
282 contractional structure F6 also emerges (Fig. 6b). As a result of such markedly
283 synchronous migration of the extensional and contractional domains, the translational
284 domain (TD3) shifts again to the area between F3 and F4 (Fig. 6b). In the landward
285 area, the extensional structures G1–G4 gradually deactivate and only G5 remains active
286 at the end of the experiment (Fig. 6b). A final shift of the translational domain occurs
287 at around 108 hours as F4 starts to extend and the area between F4 and F5 becomes part

288 of the translational domain (TD4) (Fig. 6b). Throughout the experiment, the successive,
289 short lived translational domains of Model 2 occupy a relatively small and constant area
290 (<5 % b.l.), compared to the long lived, expanding translational domain in Model 1
291 (>50 % b.l.).

292 3.3 Velocity and flow analysis

293 In both models, the surface velocity is extracted and averaged over the
294 longitudinal profiles across the silicone basins. The measured surface velocity shows a
295 local peak every time when new sediments are added in the experiment (Fig. 7a). As
296 Model 2 receives more sediments, the surface velocity is also higher. However,
297 although the sieved sediment increases gradually in both models (Fig. 2a), the averaged
298 surface velocity reaches its peak between 30 and 60 hours and then gradually decreases
299 until the end of the experiment (Fig. 7a).

300 Cross sectional views of the velocity patterns in the silicone layer derived from
301 the flow analysis demonstrate that the Poiseuille (channel) flow (e.g. Weijermars &
302 Jackson, 2014) dominate in both models, whereas Couette (shear) flow is subordinate
303 (Fig. 8). This is also reflected by the average flow velocities of both components (Fig.
304 7b) showing that the Poiseuille flow u_p is always higher than the Couette flow
305 component u_c . These results imply that the flow in the viscous layer is dominantly
306 driven by differential loading and less by shearing related to the laterally moving cover
307 wedge. Nevertheless, spatial differences in flow patterns can be observed between the
308 two models. The flow field is widely distributed in Model 1 while localized under the
309 frontal slope in Model 2 (Fig. 8). As the sediment wedge progrades, the flow field
310 expands with the wedge in Model 1, but migrates forward following the frontal slope
311 in Model 2. The averaged flow velocities reveal that the Couette flow component v_c is
312 highest between 40 and 60 hours in both models (Fig. 7a), similar to the measured
313 surface velocities (Fig. 7a). In contrast, the Poiseuille flow velocity u_p reaches its peak
314 after 80 hours in both Model 1 and 2 (Fig.7b), when the sand wedge gradually
315 progradates over the area where the silicone layer is thickest.

316 4 Discussion

317 4.1 Wedge dynamics

318 Our experiments highlight how the spreading dynamics of critically stable vs.
319 unstable progradational wedges control the structural style and kinematic evolution of
320 gravity-driven deformation in salt basins. The main problem regarding the role of
321 gravity spreading in salt tectonics is rooted in the question of whether it is alone a
322 sufficient driver for thin-skinned deformation (Brun and Fort, 2011; Rowan et al., 2012).
323 Consequently, identifying gravity spreading in nature becomes a key to solve the
324 problem. One of the main diagnostic features of gravity spreading is the development
325 of late extension over early contraction, as both domains migrate basinward along with
326 the progradational wedge (Brun and Fort, 2011; McClay et al., 1998; Vendeville, 2005).
327 Our Model 2, with a steep, unstable depositional slope, exemplifies such archetypical
328 synchronicity (Fig. 7b). In contrast, with a gentle depositional slope in Model 1, the

329 gravity spreading system is more decoupled and characterized by long lived, expanding
330 extensional and translational domains and a migrating contractional domain.

331 The kinematic evolution of Model 1 is notably similar to gravity-gliding
332 systems driven by progressive margin tilting, where the actively deforming extension
333 and contraction domains are separated by a relatively wide translational domain with
334 little internal deformation (Ge et al., 2019a; their fig. 4). However, the flow field
335 analysis shows that flow patterns in Model 1 are different from those in gravity gliding
336 systems. The latter are generally dominated by Couette flow (Brun and Fort, 2011),
337 whereas in our models Poiseuille flow exceeds the Couette flow component (Fig. 7b).
338 This indicates that horizontal redistribution of the viscous substratum and vertical
339 displacement of the cover dominates over lateral translation of the cover wedge and
340 shearing of the viscous layer (Vendeville, 2005). Temporal changes of the displacement
341 velocities (Fig. 7) suggest that the influence of both processes varies during different
342 stage of the wedge progradation. The horizontal surface and Couette velocities
343 culminate during the first half of the experiment and gradually decrease afterwards (Fig.
344 7). The Poiseuille flow velocity constantly increases and peaks in the second half of the
345 experiment. We suggest that this temporal variation of the velocities is associated with
346 the geometry of the silicone basin. Poiseuille flow velocity is generally higher, if the
347 viscous layer is thicker (Eq. 1), as the effects of boundary drag are reduced. Thus, u_p is
348 highest, where the wedge slope is the thickest within the silicone basin (Fig. 8).
349 Consequently, Poiseuille flow accelerates as the wedge progrades basinward. And the
350 pure shear deformation (“squeezing flow”; Weijermars & Jackson, 2014) in the viscous
351 layer becomes more effective than simple shear deformation, which is equivalent to
352 Couette shear flow. In another word, a larger proportion of the potential energy of the
353 wedge is translated into vertical subsidence (squeezing of the viscous layer) instead of
354 lateral translation, where the viscous layer becomes thicker.

355 The flow velocity also reveals the reason why the two wedges in Model 1 and
356 2 behave so differently. The flow velocity in Model 2 is significantly higher than Model
357 1, which results in a faster evacuation of the silicone beneath the frontal slope (Fig. 8b).
358 Thus, the overburden wedge welds quickly on the base of the silicone locking upslope
359 parts of the wedge and forcing the extensional and contractional domains to migrate
360 downslope. In contrast, the slow expulsion of silicone in Model 1 causes a long-lasting
361 deformation throughout the wedge and a relatively slow basinward migration of the
362 extensional domain (Fig. 7a). Consequently, the translational domain expands
363 continuously as the sand wedge propagates, resulting in a basin-wide deformation zone
364 (Fig. 7a).

365 4.2 Comparison with other wedge-driven gravity spreading models

366 Numerous modelling studies have focused on the gravity spreading processes
367 associated with sedimentary wedges (e.g. Adam and Krezsek, 2012; Brun and Fort,
368 2011; Ge et al., 1997; McClay et al., 2003; McClay et al., 1998; Vendeville, 2005; Yu
369 et al., 2021). Although the results of these models, including the ones in this study, can

370 be qualitatively compared, a quantitative comparison among them are rather difficult
371 due to various boundary conditions applied and modelling apparatus used. Our wedge
372 stability and silicone flow analysis allow a quantitative comparison between all models.
373 However, most published models do not provide surface velocity and deformation data.
374 Thus, the CWT and flow analysis shown here are snapshots of the wedge stability with
375 only Poiseuille flow component present (Figs 2b & 9). Furthermore, material properties
376 (e.g. density, angle of internal friction) are not always specified. Therefore, we assume
377 that materials commonly used in salt tectonic experiments are also used in these studies:
378 silicone as salt analogue (viscosity: 10^4 Pas) and quartz sand as cover (bulk density:
379 1600 kgm^3).

380 In models by McClay et al. (1998; cf. their figure 3), the frontal slope was $<5^\circ$
381 at the beginning and increased to $>10^\circ$ due to continuous sand progradation and
382 aggradation. Similar steep slopes of the progradational wedges were applied in models
383 by Yu et al. (2021; cf. their figure 6), but in combination with an initially tilted silicone
384 base. The models of both studies plot deeply in the extensionally unstable field in the
385 CWT diagram (Fig. 2b). Similar as our Model 2, zones of high-velocity Poiseuille flow
386 occur underneath the wedge front, whereas the cover already welds on the silicone base
387 in landward regions (Fig. 9a and b). Sequential cross sections in Yu et al. (2021) display
388 progressive seaward migration of the extensional domain and deactivation of landward
389 extensional structures in the late stage of the models. Thus, such evolution of the
390 deformation structures may be characteristic for gravity spreading systems with steep-
391 slope wedges.

392 In contrast, models by Ge et al. (1997; cf. their figure 6) and Vendeville (2005;
393 cf. their figure 6) applied relatively gentle slopes of roughly 5° , which plot at or close
394 to the critical state envelope in the CWT diagram (Fig. 2). Consequently, the silicone
395 flow is distributed evenly underneath the wedge (Fig. 9c and d), which is similar to the
396 flow patterns in our Model 1 (Fig. 8). Restored cross sections in Vendeville (2005; cf.
397 their figure 6) indicate that the most landward extensional structures remain active until
398 late stage of the experiment while expanding seaward. Such deformation style seems to
399 be typical for gentle-slope spreading systems as it can also be observed in our Model 1.

400 4.3 Comparison with nature

401 The two models presented here represent two endmembers of sediment-driven
402 gravity spreading systems, which can be compared to natural prototypes. The Levant
403 Basin in the eastern Mediterranean show typical features of a low-angle wedge
404 propagating over the Messinian salt layer (Cartwright and Jackson, 2008). The
405 restoration demonstrates that the sedimentary wedge had a front slope between $2.3\text{-}2.5^\circ$
406 from late Pliocene to present day (Fig. 10a). A relatively long (c. 20 km) translational
407 domain developed between the proximal extension and the distal contraction
408 (Cartwright & Jackson, 2008; their figure 9). Such a structural evolution is resembled
409 by the one observed in our Model 1 (Fig. 7a). However, the Levant margin also went
410 through a mild tilting of 0.5° . Thus, the gravity-spreading system might have been

411 slightly overprinted by gravity gliding and the salt flow may also vary through time
412 (Evans and Jackson, 2020).

413 As a contrasting example the strata in the “Albian Gap” (the Cabo Frio area),
414 located in the northern Santos Basin (Brazil), are characterised by basinward migrating
415 extension, with early extensional rafts being tens of kilometers away from the late
416 extension (Fig. 10b) (Pichel and Jackson, 2020). Such kinematic evolution is similar to
417 the migration of extension from G4 to G5 in Model 2 (Fig. 7b), suggesting a high-angle
418 frontal slope scenario. Basin physiographic analysis show that the slope of the
419 sedimentary wedges is up to 10° in the Cabo Frio area (Berton and Vesely, 2016), much
420 steeper than the surrounding area where the current slope is generally $< 1^\circ$ (Henriksen
421 et al., 2011).

422 In most cases, sedimentary progradational systems comprise various
423 depositional slopes and sediment supply varies through space and time (Carvajal et al.,
424 2009; Helland-Hansen et al., 2012; Henriksen et al., 2011). Furthermore, the associated
425 sedimentary wedges have curved topographic slopes rather than straight ones (Adams
426 and Schlager, 2000; Helland-Hansen et al., 2012). These progradational systems tend
427 to have characteristics of both endmembers during their evolution. Moreover, although
428 the two natural cases presented above show typical features of gravity spreading, other
429 factors, such as margin tilting, basin geometry, and base-salt relief may still locally or
430 temporarily affect the deformation pattern of the sedimentary wedges during their
431 evolution (Dooley et al., 2020; Pichel & Jackson, 2020). Even when dominated by
432 gravity spreading, spatial and temporal variations other than wedge geometry may also
433 play important roles in controlling the deformation. For example, as the direction of
434 sediment progradation is oblique to the (basinward) salt flow direction, the extension
435 and contraction driven by sediment wedge may superimpose on the deformation
436 parallel to the salt flow direction, forming complex salt-related structures (Guerra &
437 Underhill, 2012) or basin-scale transfer zones (Brun & Fort, 2018).

438 **5 Conclusions**

439 We use an analogue modelling approach to provide an assessment of the role of
440 gravity spreading controlled by variably steep progradational wedges in passive margin
441 salt tectonics. Our experimental results suggest that a gravity-spreading system with a
442 gentle frontal slope (close to stability in terms of force balance) is characterized by an
443 expanding extensional domain, an increasing translational domain, and basinward
444 migration of the contractional domain complimented with a more evenly distributed
445 salt flow across the basin. Such a basin evolution shares kinematic similarities with
446 gravity gliding systems that are driven by progressive margin tilting. In contrast, a
447 spreading system with a steep, mechanically unstable frontal slope induces migrating
448 extensional and contractional domains with a succession of translational domains
449 resulting in a diagnostic structural pattern. The salt flow is more localized beneath the
450 frontal slope of the wedge resulting rapid salt welding and locking of the upslope parts
451 of the wedge. In both cases, salt flow is dominated by Poiseuille flow with only a
452 subordinate contribution from Couette flow thus in contrast to classical gravity gliding

453 systems characterized by Couette flow. The Poiseuille flow increases gradually as the
454 wedge progrades to the basin centre where the silicone is thicker. Comparison with
455 other gravity spreading dominant systems with various topographic slopes shows
456 similar structural styles and silicone flow pattern. The two models presented in this
457 study are endmembers of gravity spreading systems. Natural cases may show hybrid
458 characters depending on the wedge stability. Other factors, such as margin tilting, salt
459 thickness and base-salt relief may further complicate the deformation. Our study has
460 important implications in interpreting thin-skinned salt tectonic deformation. For
461 example, the downward migration of the extensional domain hints to a steep slope
462 system, as it can be observed in the Santos Basin. However, such steep slope systems
463 may not be very common in salt-bearing passive margins compare to their gentle slope
464 counterparts due to their less likely occurrence in sedimentary systems.

465 **Acknowledgments**

466 ZG thanks the Science Foundation of China University of Petroleum, Beijing (No.
467 2462020QNXZ002) and L. Meltzers Høyskolefond for financial support. Frank
468 Neumann and Thomas Ziegenhagen are thanked for technical assistance. We thank
469 Nadaya Cubas for providing the script of the CWT analysis. We thank Jonathan
470 Bedford for reading an early draft of this paper. GFZ Data Services are thanked for
471 making the data openly accessible.

472 [Experimental data of this study will be published open access in Ge et al. \(2021\): temporary preview](#)
473 [link: https://dataservices.gfz-](https://dataservices.gfz-potsdam.de/panmetaworks/review/297eadbaf7749a95ba2805adcd7602081bf9bceef5fbbc5afc423f43810f0058/)
474 [potsdam.de/panmetaworks/review/297eadbaf7749a95ba2805adcd7602081bf9bceef5fbbc5afc423f4381](https://dataservices.gfz-potsdam.de/panmetaworks/review/297eadbaf7749a95ba2805adcd7602081bf9bceef5fbbc5afc423f43810f0058/)
475 [0f0058/](https://dataservices.gfz-potsdam.de/panmetaworks/review/297eadbaf7749a95ba2805adcd7602081bf9bceef5fbbc5afc423f43810f0058/)

476

477 **References**

- 478 Adam, J., Z. Ge, and M. Sanchez, 2012, Post-rift salt tectonic evolution and key
479 control factors of the Jequitinhonha deepwater fold belt, central Brazil passive
480 margin: Insights from scaled physical experiments: *Marine and Petroleum*
481 *Geology*, v. 37, p. 70–100.
- 482 Adam, J., and C. Krezsek, 2012, Basin-scale salt tectonic processes of the Laurentian
483 Basin, Eastern Canada: insights from integrated regional 2D seismic
484 interpretation and 4D physical experiments: Geological Society, London,
485 *Special Publications*, v. 363, p. 331–360.
- 486 Adam, J., J. L. Urai, B. Wieneke, O. Oncken, K. Pfeiffer, N. Kukowski, J. Lohrmann,
487 S. Hoth, W. van der Zee, and J. Schmatz, 2005, Shear localisation and strain
488 distribution during tectonic faulting—new insights from granular-flow
489 experiments and high-resolution optical image correlation techniques: *Journal*
490 *of Structural Geology*, v. 27, p. 283–301.
- 491 Adams, E. W., and W. Schlager, 2000, Basic Types of Submarine Slope Curvature:
492 *Journal of Sedimentary Research*, v. 70, p. 814–828.

- 493 Allen, H., C. A.-L. Jackson, and A. J. Fraser, 2016, Gravity-driven deformation of a
494 youthful saline giant: the interplay between gliding and spreading in the
495 Messinian basins of the Eastern Mediterranean: *Petroleum Geoscience*, v. 22,
496 p. 340-356.
- 497 Berton, F., and F. F. Vesely, 2016, Seismic expression of depositional elements
498 associated with a strongly progradational shelf margin: northern Santos Basin,
499 southeastern Brazil: *Brazilian Journal of Geology*, v. 46, p. 585-603.
- 500 Brun, J.-P., and X. Fort, 2011, Salt tectonics at passive margins: Geology versus
501 models: *Marine and Petroleum Geology*, v. 28, p. 1123–1145.
- 502 Byerlee, J., 1978, Friction of rocks, *in* J. D. Byerlee, and M. Wyss, eds., *Rock friction
503 and earthquake prediction: Contributions to Current Research in Geophysics
504 (CCRG): Birkhäuser, Basel, Springer*, p. 615–626.
- 505 Cartwright, J. A., and M. P. A. Jackson, 2008, Initiation of gravitational collapse of an
506 evaporite basin margin: The Messinian saline giant, Levant Basin, eastern
507 Mediterranean: *Geological Society of America Bulletin*, v. 120, p. 399-413.
- 508 Carvajal, C., R. Steel, and A. Petter, 2009, Sediment supply: The main driver of shelf-
509 margin growth: *Earth-Science Reviews*, v. 96, p. 221–248.
- 510 Cobbold, P. R., and P. Szatmari, 1991, Radial gravitational gliding on passive
511 margins: *Tectonophysics*, v. 188, p. 249–289.
- 512 Cohen, H. A., and S. Hardy, 1996, Numerical modelling of stratal architectures
513 resulting from differential loading of a mobile substrate, *in* G. I. Alsop, D. J.
514 Blundell, and I. Davison, eds., *Salt Tectonics*, v. 100, Geological Society,
515 London, Special Publications, p. 265–273.
- 516 Dooley, T. P., M. R. Hudec, L. M. Pichel, and M. P. A. Jackson, 2020, The impact of
517 base-salt relief on salt flow and suprasalt deformation patterns at the
518 autochthonous, paraautochthonous and allochthonous level: insights from
519 physical models: Geological Society, London, Special Publications, v. 476.
- 520 Evans, S., and C. A.-L. Jackson, 2021, Intrasalt Structure and Strain Partitioning in
521 Layered Evaporites: Implications for Drilling Through Messinian Salt in the
522 Eastern Mediterranean: *Petroleum Geoscience*, online first.
- 523 Fort, X., J.-P. Brun, and F. Chauvel, 2004, Salt tectonics on the Angolan margin,
524 synsedimentary deformation processes: *AAPG bulletin*, v. 88, p. 1523–1544.
- 525 Ge, H., M. P. A. Jackson, and B. C. Vendeville, 1997, Kinematics and dynamics of
526 salt tectonics driven by progradation: *AAPG bulletin*, v. 81, p. 398–423.
- 527 Ge, Z., M. Warsitzka, M. Rosenau, and R. L. Gawthorpe, 2019a, Progressive tilting of
528 salt-bearing continental margins controls thin-skinned deformation: *Geology*,
529 v. 47, p. 1122-1126.
- 530 Ge, Z., M. Rosenau, M. Warsitzka, and R. L. Gawthorpe, 2019b, Overprinting
531 translational domains in passive margin salt basins: insights from analogue
532 modelling: *Solid Earth*, v. 10, p. 1283-1300.
- 533 Gemmer, L., C. Beaumont, and S. J. Ings, 2005, Dynamic modelling of passive
534 margin salt tectonics: effects of water loading, sediment properties and
535 sedimentation patterns: *Basin Research*, v. 17, p. 383–402.

- 536 Gradmann, S., C. Beaumont, and M. Albertz, 2009, Factors controlling the evolution
537 of the Perdido Fold Belt, northwestern Gulf of Mexico, determined from
538 numerical models: *Tectonics*, v. 28.
- 539 Helland-Hansen, W., R. J. Steel, and T. O. Sømme, 2012, Shelf genesis revisited:
540 *Journal of Sedimentary Research*, v. 82, p. 133–148.
- 541 Henriksen, S., W. Helland-Hansen, and S. Bullimore, 2011, Relationships between
542 shelf-edge trajectories and sediment dispersal along depositional dip and
543 strike: a different approach to sequence stratigraphy: *Basin Research*, v. 23, p.
544 3–21.
- 545 Howlett, D., R. Gawthorpe, Z. Ge, A. Rotevatn, and C. A.-L. Jackson, 2021,
546 Turbidites, Topography and Tectonics: Evolution of submarine channel-lobe
547 systems in the salt-influenced Kwanza Basin, offshore Angola: *Basin*
548 *Research*, v. 33, p.1076–1110.
- 549 Hudec, M. R., and M. P. Jackson, 2007, Terra infirma: Understanding salt tectonics:
550 *Earth-Science Reviews*, v. 82, p. 1–28.
- 551 Ings, S., C. Beaumont, and L. Gemmer, 2004, Numerical modeling of salt tectonics on
552 passive continental margins: Preliminary assessment of the effects of sediment
553 loading, buoyancy, margin tilt, and isostasy: *Perkins Research Conference*, p.
554 36–68.
- 555 Kehle, R. O., 1988, The origin of salt structures, *in* B. C. Schreiber, ed., *Evaporites*
556 *and Hydrocarbons: New York, Columbia University Press*, p. 345–404.
- 557 Klinkmüller, M., G. Schreurs, M. Rosenau, and H. Kemnitz, 2016, Properties of
558 granular analogue model materials: A community wide survey:
559 *Tectonophysics*, v. 684, p. 23–38.
- 560 Krézsek, C., J. Adam, and D. Grujic, 2007, Mechanics of fault and expulsion rollover
561 systems developed on passive margins detached on salt: insights from
562 analogue modelling and optical strain monitoring: *Geological Society,*
563 *London, Special Publications*, v. 292, p. 103–121.
- 564 Kukla, P. A., F. Strozyk, and W. U. Mohriak, 2018, South Atlantic salt basins –
565 Witnesses of complex passive margin evolution: *Gondwana Research*, v. 53, p.
566 41–57.
- 567 Lugo-Fernández, A., and M. M. Morin, 2004, Slope and Roughness Statistics of the
568 Northern Gulf of Mexico Seafloor With Some Oceanographic Implications:
569 *Gulf of Mexico Science*, v. 22.
- 570 McClay, K., T. Dooley, and G. Zamora, 2003, Analogue models of delta systems
571 above ductile substrates: *Geological Society London Special Publications*, v.
572 216, p. 411–428.
- 573 McClay, K. R., T. Dooley, and G. Lewis, 1998, Analog modeling of progradational
574 delta systems: *Geology*, v. 26, p. 771–774.
- 575 Mourgues, R., A. Lacoste, and C. Garibaldi, 2014, The Coulomb critical taper theory
576 applied to gravitational instabilities: *Journal of Geophysical Research: Solid*
577 *Earth*, v. 119, p. 754–765.
- 578 Nemec, W., 1990, Aspects of Sediment Movement on Steep Delta Slopes, *in* A.
579 Colella, and D. Prior, eds., *Coarse-Grained Deltas*, *International Association*
580 *of Sedimentologist Special Publication*, p. 29–73.

- 581 O'Grady, D. B., J. P. M. Syvitski, L. F. Pratson, and J. F. Sarg, 2000, Categorizing the
582 morphologic variability of siliciclastic passive continental margins: *Geology*,
583 v. 28, p. 207–210.
- 584 Patruno, S., and W. Helland-Hansen, 2018, Clinofolds and clinofold systems:
585 Review and dynamic classification scheme for shorelines, subaqueous deltas,
586 shelf edges and continental margins: *Earth-Science Reviews*, v. 185, p. 202–
587 233.
- 588 Peel, F., 2014, The engines of gravity-driven movement on passive margins:
589 Quantifying the relative contribution of spreading vs. gravity sliding
590 mechanisms: *Tectonophysics*, v. 633, p. 126–142.
- 591 Pichel, L. M., and C. A. Jackson, 2020, The Enigma of the Albian Gap: Spatial
592 Variability and the Competition Between Salt Expulsion and Extension:
593 *Journal of the Geological Society*, v. 177, 1129–1148.
- 594 Prather, B. E., C. O'Byrne, C. Pirmez, and Z. Sylvester, 2017, Sediment partitioning,
595 continental slopes and base-of-slope systems: *Basin Research*, v. 29, p. 394–
596 416.
- 597 Quirk, D. G., N. Schødt, B. Lassen, S. J. Ings, D. Hsu, K. K. Hirsch, and C. Von
598 Nicolai, 2012, Salt tectonics on passive margins: examples from Santos,
599 Campos and Kwanza basins: Geological Society, London, Special
600 Publications, v. 363, p. 207–244.
- 601 Raillard, S., B. C. Vendeville, and G. Gue'rin, 1997, Causes and structural
602 characteristics of thin-skinned inversion during gravity gliding or spreading
603 above salt or shale, AAPG Annual Convention Official Program, p. A95.
- 604 Roberts, H., R. McBride, and J. Coleman, 1999, Outer shelf and slope geology of the
605 Gulf of Mexico: an overview: *The Gulf of Mexico Large Marine Ecosystem*:
606 Blackwell Science.
- 607 Ross, W., B. Halliwell, J. May, D. Watts, and J. Syvitski, 1994, Slope readjustment: a
608 new model for the development of submarine fans and aprons: *Geology*, v. 22,
609 p. 511–514.
- 610 Rowan, M. G., 2020, Salt- and shale-detached gravity-driven failure of continental
611 margins: *Regional Geology and Tectonics* (Second Edition).
- 612 Rowan, M. G., F. J. Peel, and B. C. Vendeville, 2004, Gravity-driven fold belts on
613 passive margins, *in* K. R. McClay, ed., *Thrust tectonics and hydrocarbon*
614 *systems*, AAPG Memoir, p. 157–182.
- 615 Rowan, M. G., F. J. Peel, B. C. Vendeville, and V. Gaullier, 2012, Salt tectonics at
616 passive margins: *Geology versus models—Discussion: Marine and Petroleum*
617 *Geology*, v. 37, p. 184–194.
- 618 Rudolf, M., D. Boutelier, M. Rosenau, G. Schreurs, and O. Oncken, 2016,
619 Rheological benchmark of silicone oils used for analog modeling of short-and
620 long-term lithospheric deformation: *Tectonophysics*, v. 684, p. 12–22.
- 621 Schlager, W., and O. Camber, 1986, Submarine slope angles, drowning
622 unconformities, and self-erosion of limestone escarpments: *Geology*, v. 14, p.
623 762–765.
- 624 Schultz-Ela, D. D., 2001, Excursus on gravity gliding and gravity spreading: *Journal*
625 *of Structural Geology*, v. 23, p. 725–731.

- 626 Turcotte, D., and G. Schubert, 2014, *Geodynamics* (3rd ed.): Cambridge, Cambridge
627 University Press.
- 628 Vendeville, B. C., 2005, Salt tectonics driven by sediment progradation: Part I—
629 Mechanics and kinematics: *AAPG bulletin*, v. 89, p. 1071–1079.
- 630 Warsitzka, M., Z. Ge, J.-M. Schönebeck, A. Pohlenz, and N. Kukowski, 2019, Ring-
631 shear test data of foam glass beads used for analogue experiments in the
632 Helmholtz Laboratory for Tectonic Modelling (HelTec) at the GFZ German
633 Research Centre for Geosciences in Potsdam and the Institute of Geosciences,
634 Friedrich Schiller University Jena, GFZ Data Services.
- 635 Warsitzka, M., N. Kukowski, and J. Kley, 2018, Salt flow direction and velocity
636 during subsalt normal faulting and syn-kinematic sedimentation—implications
637 from analytical calculations: *Geophysical Journal International*, v. 213, p. 115–
638 134.
- 639 Weijermars, R., and M. P. Jackson, 2014, Predicting the depth of viscous stress peaks
640 in moving salt sheets: Conceptual framework and implications for drilling:
641 *AAPG bulletin*, v. 98, p. 911–945.
- 642 Yu, Y., C. Tao, S. Shi, J. Yin, C. Wu, and J. Liu, 2021, Physical modeling of salt
643 structures in the middle south Atlantic marginal basins and their controlling
644 factors: *Petroleum Exploration and Development*, v. 48, p. 136–145.
- 645 Zucker, E., Z. Gvirtzman, J. Steinberg, and Y. Enzel, 2019, Salt tectonics in the
646 Eastern Mediterranean Sea: Where a giant delta meets a salt giant: *Geology*, v.
647 48, p. 134–138.
- 648 Zwaan, F., M. Rosenau, and D. Maestrelli, 2021, How initial basin geometry
649 influences gravity-driven salt tectonics: Insights from laboratory experiments:
650 *Marine and Petroleum Geology*, p. 105195.

651

652 **Figure and table caption**

653 **Figure 1.** (a) Gravity gliding vs. (b) gravity spreading systems (modified after Allen
654 et al., 2016). Both deformation modes are generally associated with a landward
655 extension and a seaward shortening as well as lateral redistribution of the salt.

656 **Figure 2.** Wedge stability analysis using Critical Wedge Theory (CWT) (Dahlen,
657 1990). (a) The two wedge geometries applied in our study and various wedge
658 geometries of previous studies are plotted together with the CWT predicted stability
659 fields. The two curves correspond to viscous strength equivalent basal friction angles
660 of 0.1° and 1° (red = 0.1° , green = 1°) representing the expected range of basal
661 strength. (b) Zoom into the CWT model domain.

662 **Figure 3.** Cross-sectional (a) and plane view (b) of the model design. A gentle-slope
663 wedge ($\sim 5^\circ$) is applied in Model 1 and a steep-slope wedge ($\sim 27^\circ$) in Model 2.

664 **Figure 4.** Schematic diagram of flow analysis based on the setup of the presented
665 analogue experiments. The sand wedge on top of the silicone layer induces a

666 Poiseuille channel flow (u_p). Due to the redistribution of the silicone, the sand wedge
667 collapses gravitationally, which means it subsides into the silicone layer and slides
668 laterally. The lateral sliding with the velocity u_T causes a Couette shear flow
669 component (u_c) overlapping with the Poiseuille flow.

670 **Figure 5.** Map views of incremental longitudinal surface strain (ϵ_{xx}) in Model 1 (a)
671 and 2 (b) at early (9–10 h), intermediate (49–50 h) and late (89–90 h) stages during
672 the experiment.

673 **Figure 6.** (a) Middle cross section and the associated longitudinal surface strain rate
674 map of Model 1. Note the expansion of extensional and translational domains as well
675 as the basinward migration of the contractional domain. (b) Middle cross section and
676 the associated longitudinal surface strain rate map of Model 2. Note the synchronized
677 basinward migration of both extension and contraction and the shifts of the
678 translational domain (TD). Strain rate maps are constructed by plotting strain rate (1 h
679 increments) along the middle profile (x axis) over time (y axis).

680 **Figure 7.** (a) Surface velocity averaged profile vs. time for Model 1 and 2 along the
681 middle section. The dashed lines represent the actually measured velocities derived
682 from the DIC analysis, whereas the solid line is the moving average. (b) Average
683 values of the Poiseuille flow u_p and Couette flow velocity u_c derived from the silicone
684 flow analysis for each phase of sedimentation. In both models, Poiseuille flow
685 dominates over Couette flow.

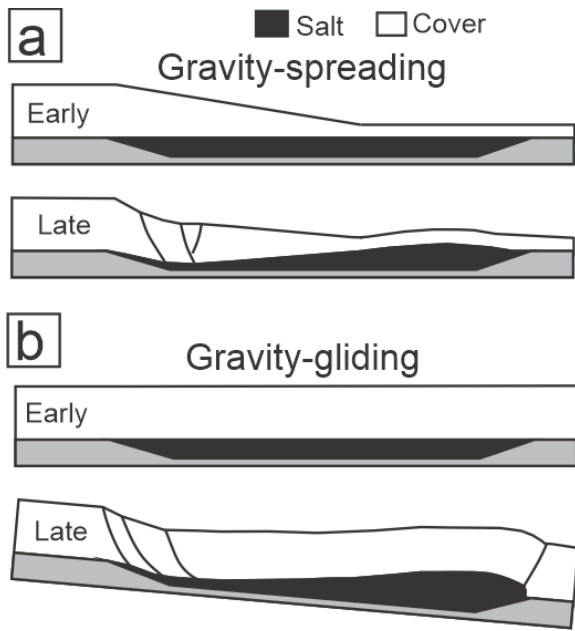
686 **Figure 8.** Representative cross sections showing the velocity field in the silicone and
687 the cover layer from early (13–24 h), mid (37–48h) and late (61–72h) stages during
688 model evolution. Silicone flow is widely distributed in Model 1, whereas it is focused
689 beneath the frontal edge of the wedge in Model 2.

690 **Figure 9.** Representative cross sections of previous analogue modelling studies on
691 gravity spreading showing the Poiseuille flow patterns in the viscous layer. Cross
692 sections derived from the literature are used as input for the silicone flow analysis. (a)
693 Flow patterns in the viscous layer based on cross sections of Model 1 and Model 2 in
694 McClay et al. (1998). Poiseuille flow is fastest beneath the wedge front. (b) Flow
695 patterns based on cross sections of two successive stage of Model 1 in Yu et al.(2021).
696 The base of the silicone is tilted with 5° . (c) Flow patterns based on restored cross
697 sections of two stage of Model 1 in Ge et al. (1997). Note the relatively even
698 distribution of silicone flow beneath wedge in profile 1 and more localized flow in
699 profiles 2. (d) Flow patterns based restored cross sections of the model shown in
700 Vendeville (2005). Note the relatively even distribution of the viscous flow beneath
701 the wedge.

702 **Figure 10.** (a) Cross section along the Levant margin in the eastern Mediterranean
703 Sea. Note the translational domain in the mid slope and its overall similarity to Model
704 1 (modified from Fig. 9 in Cartwright & Jackson, 2008). (b) South–central section
705 from the Albian Gap (the Cabo Frio Fault). Note the early and late (migrated)

706 extension and possible early contraction (modified from Fig. 7 in Pichel & Jackson,
707 2020).

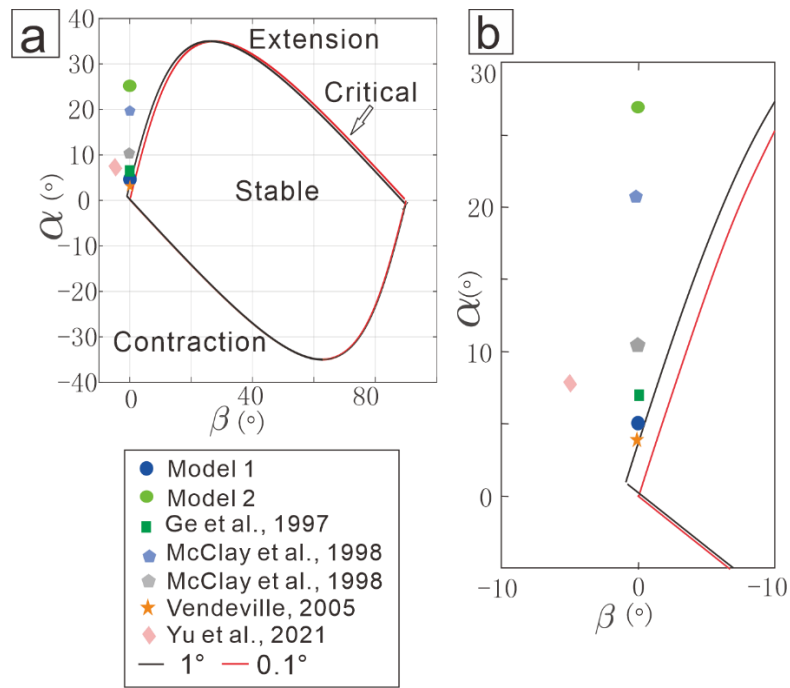
708 **Table 1.** Material properties and scaling parameters of the experiments. Geometric
709 scaling of 1cm in model is 1 km in nature. Time scaling of 1 h in model is 0.268 Ma
710 in nature. For full details of the scaling, see (Adam et al., 2012).
711



712

713 Figure 1

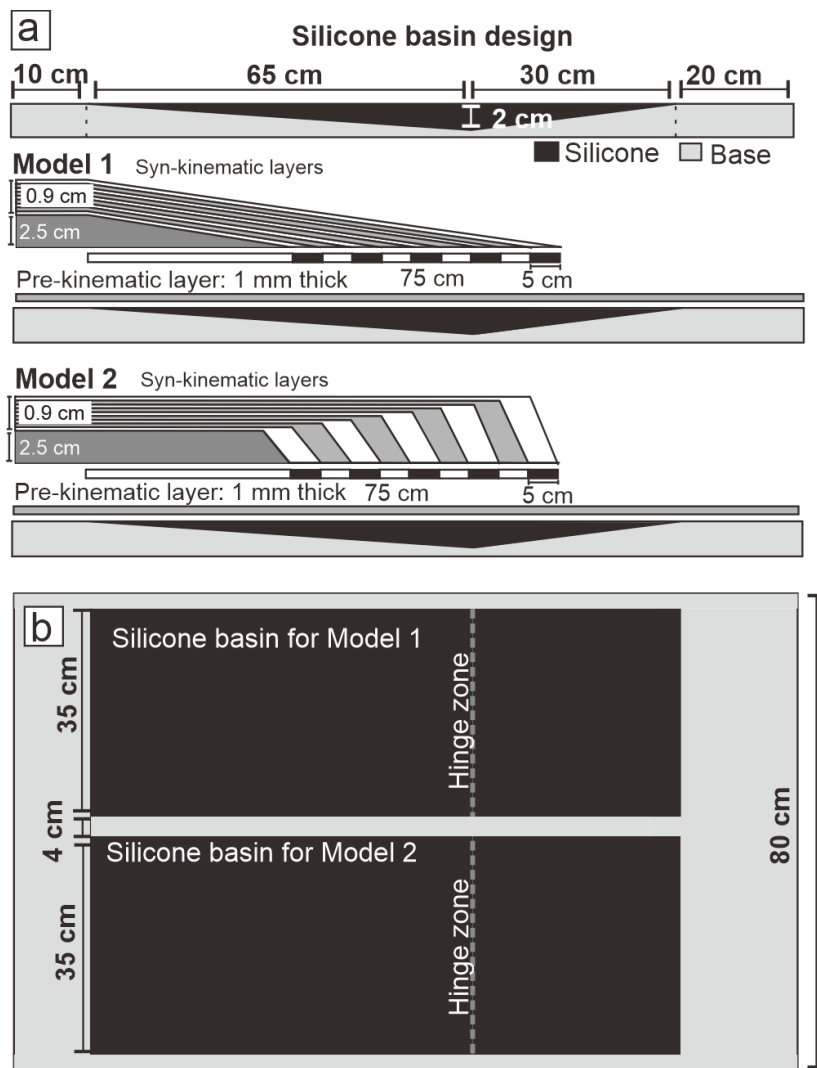
714



715

716 Figure 2

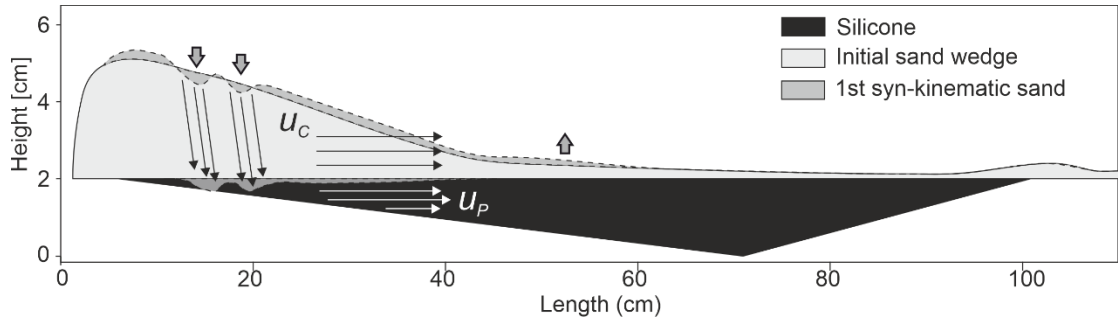
717



718

719 Figure 3

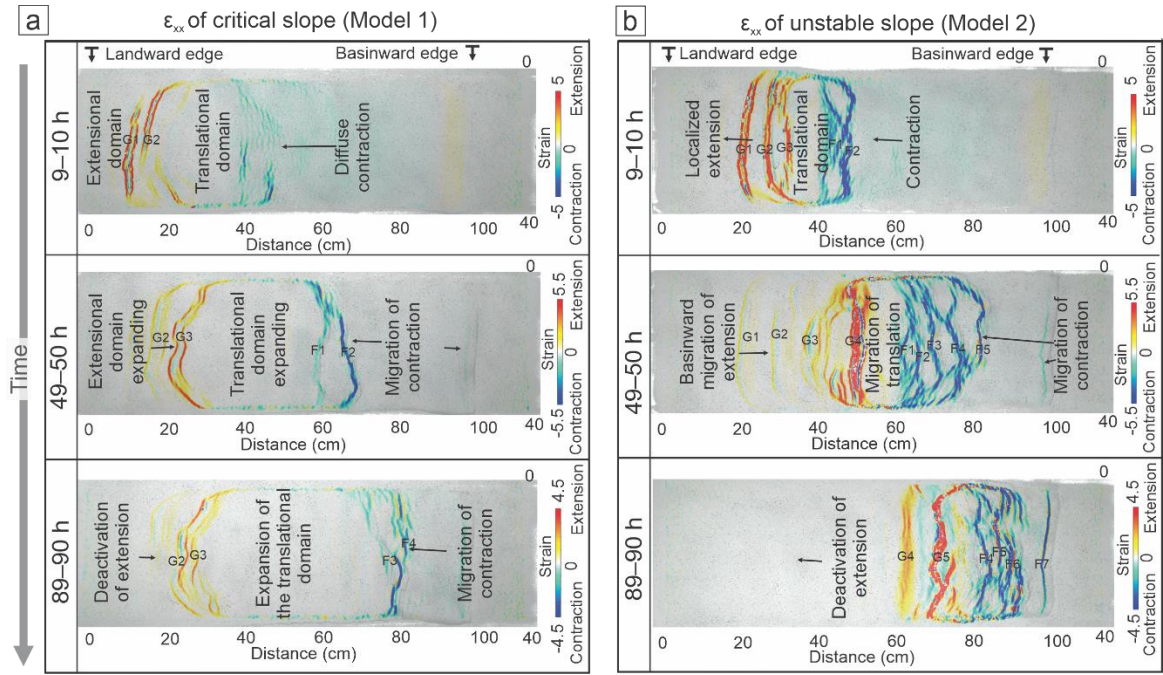
720



721

722 Figure 4

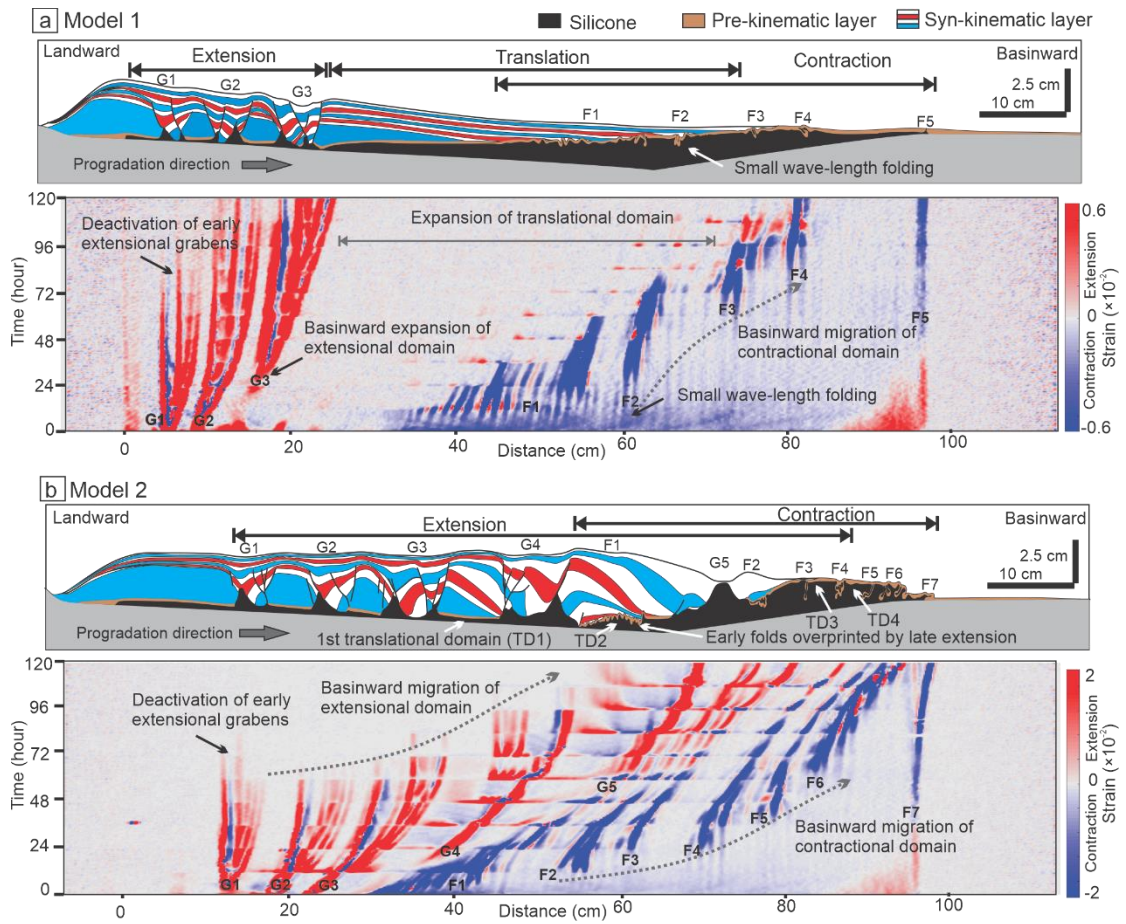
723



724

725 Figure 5

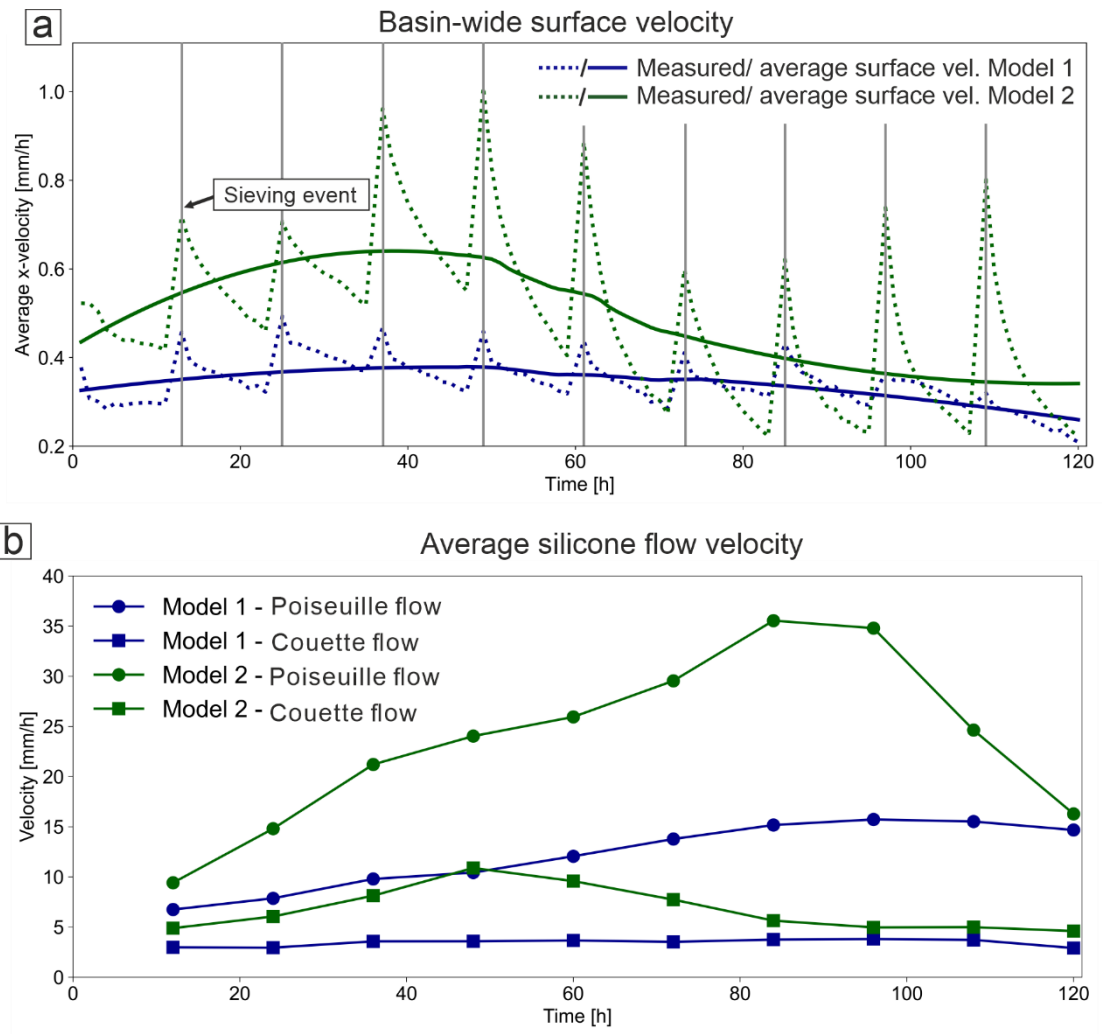
726



727

728 Figure 6

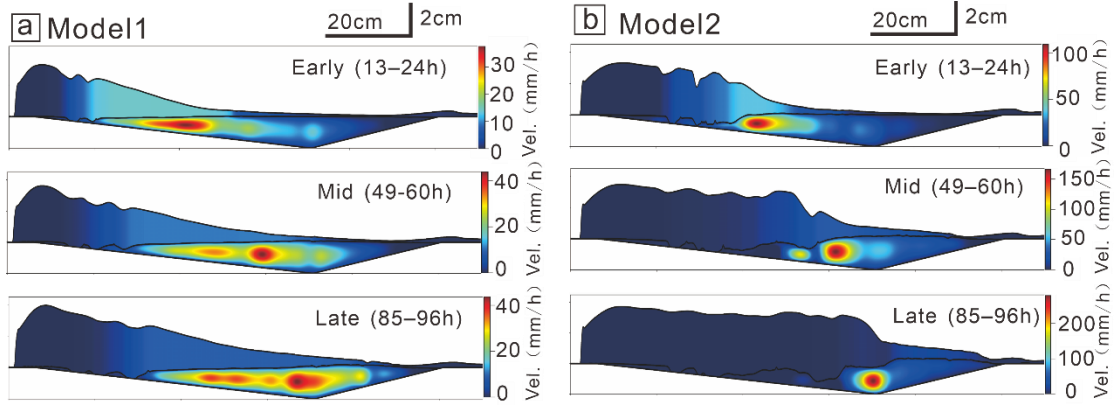
729



730

731 Figure 7

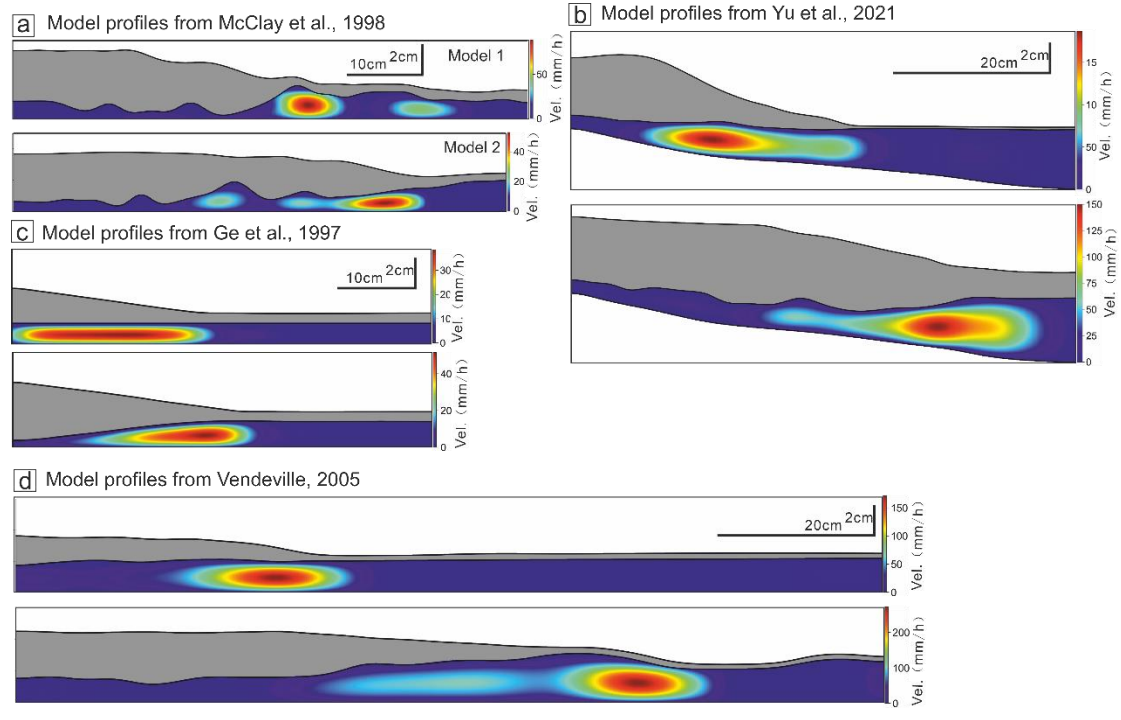
732



733

734 Figure 8

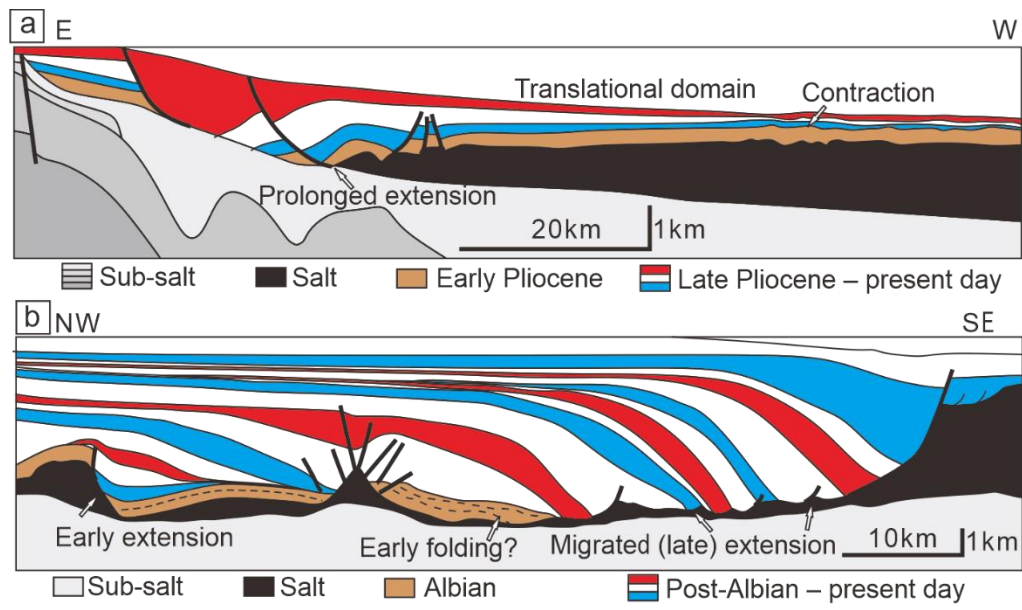
735



736

737 Figure 9

738



739

740 Figure 10

741

Scaling table:

Quantity	Symbol	Unit	Value (model)	Value (prototype)	Scaling relation	Scaling factor
Length	l	m	0.01	1	$l^* = l_{\text{model}}/l_{\text{prototype}}$	10^{-5}
Density overburden	ρ_c	$kg \cdot m^{-3}$	1130	2400	$\rho_c^* = \rho_{c \text{ model}}/\rho_{c \text{ prototype}}$	0.47
Gravity acceleration	g	$m \cdot s^{-2}$	9.81	9.81	$g^* = g_{\text{model}}/g_{\text{prototype}}$	1
Friction coefficient [#]	μ	-	0.55–0.75	0.40–0.80	$\mu^* = \mu_{\text{model}}/\mu_{\text{prototype}}$	1
Cohesion [#]	C	Pa	35–75	10^7	$C^* = \rho_c^* l^* g^*$	10^{-5}
Stress	σ	Pa	100 2.00	21.30×10^6	$\sigma^* = \rho_c^* l^* g^*$	4.70×10^{-6}
Viscosity*	η	$Pa \cdot s$	$\times 10^4$	5.00×10^{18}	$\eta^* = \eta_{\text{model}}/\eta_{\text{prototype}}$	4.00×10^{-15}
Strain rate	ϵ	s^{-1}	10^{-2} – 10^{-7}	10^{-11} – 10^{-16}	$\epsilon^* = \sigma^*/\eta^*$	1.18×10^9
Time (subaerial) Time (submarine)	t_a t_m	h h	1	1.18×10^9 2.35×10^9	$t_a^* = 1/\epsilon^*$ $t_m^* = 0.5 t_a^*$	8.51×10^{-10} 4.26×10^{-10}

[#]For static>reactivation>dynamic friction coefficients (Warsitzka et al., 2019)

*Viscosity after Rudolf et al. (2016)

742

743 Table 1